Introducing drone-based GPR in snow hydrology studies

Eole Valence[1,2], Michel Baraer[1,2], Eric Rosa[2,3], Florent Barbecot[2,4], Chloe Monty[1]

[1]Departement de genie de la construction, Ecole de Technologie Superieure, Montreal, H3C 1K3, Canada
[2]Geotop, Montreal, H2X 3Y7, Canada
5 [3]Groupe de recherche sur l'eau souterraine, Universite du Quebec en Abitibi-Temiscamingue, Rouyn-Noranda, J9X 5E4, Canada
[4]Departement des sciences de la Terre et de l'atmosphere, Universite du Quebec a Montreal, Montreal, H2L 2C4, Canada

Correspondence to: Eole Valence (eole.valence.1@ens.etsmtl.ca)

Abstract. Seasonal snowpack deeply influences the distribution of meltwater among watercourses and groundwater. During
10 rain-on-snow (ROS) events, for instance, the structure and properties of the different ice and snow layers dictate the quantity of water flowing out of the snowpack, increasing the risk of flooding and ice jams. With ongoing climate change, a better understanding of the processes and internal properties influencing snowpack outflows is needed to predict the hydrological consequences as mild episodes and ROS events' frequency increases. This study aims to develop a multi-method approach to monitor the key snowpack properties in a non-mountainous environment in a repetitive and non-destructive way. Snowpack
15 evolution was evaluated using a combination of drone-based GPR, photogrammetry surveys and time domain reflectometry (TDR) measurements, tested during the winter of 2020–2021 at the Sainte-Marthe experimental watershed, Quebec, Canada. The experimental watershed is equipped with state-of-the-art automatic weather stations that, together with weekly snow pit measurements, serve as a reference for the multi-method monitoring approach. Drone surveys conducted on a weekly basis are used to generate georeferenced snow depth, relative density, snow water equivalent and average liquid water content
20 maps. In between site visits, snowpack properties are monitored using TDR probes.

Despite some limitations, the results show that the approach is very promising in assessing the spatiotemporal evolution of the key hydrological characteristics of the snowpack. Among others, results showed the prevalence of preferential pathways at the early stage of the ablation period, the difference in hydrological reaction to a ROS event between flat and sloped sections of the study area and the hydrological influence of solar radiation at the late stage of the ablation period.

25 ## 1 Introduction

The seasonal snow cover is of great hydrological influence in cold regions. By acting as seasonal transient storage, it determines the amplitude of spring floods, the level of late summer flows and the recharge of aquifers (Dewalle and Rango, 2008). Snowmelt floods are a cause of economic losses and sometimes loss of life (Ding et al., 2021), while insufficient aquifer recharge impacts water availability for agricultural and industrial uses, fresh water supply and the ecology of river
30 systems (Dierauer et al., 2021).

Economic sectors, such as hydroelectricity production (Brown et al., 2018) and agriculture (Liu and Lobb, 2021) show high vulnerability to changes in the snow cover and related hydrological impacts. Changes in snow cover characteristics have been reported from cold regions. For example, a decline in snow-covered area has been observed over the Tibetan plateau (Zhang et al., 2015), along with losses in snowpack water storage in Europe (Magnusson et al., 2010), densification of

35 snowpack in eastern North America (Hodgkins and Dudley, 2006; Ford et al., 2021) and decline of spring snow cover in western Canada (Najafi et al., 2017). Climate change projections anticipate a further alteration of snowpack characteristics. Due to climate change, seasonal snowpack depth is expected to diminish (Dierauer et al., 2021), the winter maximum snow water equivalent to decline (Sun et al., 2019) and the spring melt to occur earlier in the season (Gergel et al., 2017).

Moreover, observations and models indicate an increase in the number of rain-on-snow (ROS) events during the winter (Li

40 et al., 2019). Combined with changes in snowpack characteristics, those events are predicted to trigger an increase in winter flood and ice jam intensity and frequency (Morse and Turcotte, 2018; Andradóttir et al., 2021).

Snowpack physical characteristics and hydrological behavior are deeply interrelated (Mas et al., 2018). While the snowpack structure controls internal water fluxes, liquid water movement, storage and phase change in the snowpack transform and modify that structure (Quéno et al., 2020). Within this context, monitoring the spatiotemporal evolution of snow cover

45 properties appears essential for anticipating adverse climate change consequences on winter hydrology and groundwater recharge (Lindström et al., 2010).

Snow depth (h), density (ρ), snow water equivalent (SWE) and liquid water content (LWC) are among the most measured physical quantities of the snowpack (Kinar and Pomeroy, 2015a). These four variables are considered as key properties for characterizing the snowpack's hydrological behavior (Vionnet et al., 2021) and show high variability in time and in space,

50 making them difficult to capture at the appropriate scale.

Snow depth is widely monitored using ultrasonic sensors, with an accuracy of 2 cm (Doesken et al., 2008). More recently, h measurements using Global Navigation Satellite System Interferometric Reflectometry (GNSS-IR) have grown in popularity (Chen et al., 2021). Terrestrial laser scanning has been successfully used for h distributed measurements with a vertical accuracy of 10 cm (Prokop, 2008; Revuelto et al., 2015; Deems et al., 2017). Airborne photogrammetry shows great

55 potential for h measurement. With a centimeter scale accuracy, this technique allows for the non-destructive monitoring of the spatial variability of h (Bühler et al., 2016a). However, airborne photogrammetry application is limited to open environments (Harder et al., 2020). By contrast, airborne lidar (light detection and ranging) h measurements have proven to be efficient in forest environments (Koutantou et al., 2021). Even with growing access to those remote measurement techniques, destructive manual measurements remain extensively used for snow monitoring (Leppänen et al., 2016).

60 Indeed, h measurement using rods and rules is still seen as a reference to capture h spatial variability and/or to validate remote sensing measurements (Kinar and Pomeroy, 2015b).

Snow density is commonly measured through gravimetric measurements or calculated from h and SWE measurements (Conger and Mcclung, 2009). In dry conditions, snow density can be estimated with a dielectric permittivity measurement systems such as the Finnish SnowFork (Hao et al., 2021). Other methods include time domain reflectometry (TDR), ground-

65 penetrating radar measurement (Previati et al., 2011), neutron probe (Hawley et al., 2008) and diffuse near-infrared transmission (Gergely et al., 2010).

Different methods are used to measure the spatial variation of *SWE*. Manual measurements consist of snow-coring to estimate sample volume and mass. The manual method is time-consuming, destructive, and of moderate precision (Sturm and Holmgren, 2018). Where hard layers are present, sequential sampling is required, making the method more labor

70 intensive (Morris and Cooper, 2003; Paquotte and Baraer, 2022). Manual methods are subject to operational sampling errors and bias (Goodison et al., 1987). Automatic monitoring makes it possible to capture *SWE* variability temporally. The methods most often used are gamma ray monitoring (GMON), cosmic ray neutron probe (CNRP), snow pillows and plates, the system for acoustic sensing of snow (SAS2) and the snowpack analyzer (SPA-2). GMON and CNRP require site calibration, and the stationary version of SAS2 has a limited footprint (2–3 m of diameter) (Kinar and Pomeroy, 2015a;

75 Royer et al., 2021). Moreover, the high price of automatic monitoring systems limit their large-scale deployment. Snow pillows and plates are limited to flat areas, while freeze and thaw events may affect their functioning. GNSS receiver-based *SWE* estimations are an emerging alternative to the above-mentioned automatic measurement systems. However, they still require calibration using a reference method (Yu et al., 2020). The use of satellite-based remote sensing for *SWE* measurement has received much attention over the past decade. For example, repetitive L-band measurements allow the

80 InSAR applications to map *SWE* over large areas (Rott et al., 2003). However, the method still needs some improvements for application in wooded areas. Passive microwave remote sensing provides information over large areas on snow mass, which can be related to *SWE* (Foster et al., 2005). Thus, it provides coarse spatial data with a high degree of uncertainty (Mortimer et al., 2020).

The most common in situ *LWC* measurement methods are based on snow dielectric constant measurements at single points

85 of the snowpack. The SnowFork (Sihvola and Tiuri, 1986), the Denoth device (Denoth, 1995) and the A2 Photonic WISe sensor (Webb et al., 2021) are among the most popular devices to measure *LWC*. They all present an accuracy of around 1% of the volumetric *LWC*. The most accurate method, often used as a reference for those devices is freezing or melting calorimetry (Mavrovic et al., 2020). *LWC* may be monitored with radar (Lundberg et al., 2013), TDR (Lundberg et al., 2016) or devices such as SAS2 and SPA-2.

90 So far, taken individually none of the methods presented here above can capture the spatiotemporal variability of the snowpack's hydrological behavior at representative scales.

Combining techniques that monitor the temporal evolution of the snow permittivity at a sub-hourly time step such as TDR, with those mapping its variation in space such as GPR is therefore seen as a promising approach to address this challenge (Godio et al., 2018). Different empirical fuctions have been developed to relate ρ and *LWC* to the measured permittivity (Di

95 Paolo et al., 2018; Frolov and Macheret, 1999). In dry conditions, *LWC* can be neglected, leaving a direct relation between ρ and the relative permittivity. In wet conditions, either assumptions are made on ρ variability from spot measurements (e.g., Webb et al. (2020); Yildiz et al. (2021)) or ρ maps must be produced using a separate method. In that regard, the *LWC* estimation from frequency-dependent attenuation of the GPR signal proposed by (Bradford et al., 2009) shows great

potential. As *SWE* can be calculated from ρ and h, measuring h from methods such as drone-based photogrammetry or lidar
100 can provide more direct and precise *SWE* estimation (Lundberg et al., 2016).

One of the main drawbacks of using GPR over the snowpack is the required contact between the GPR carrier and the snow,
which affects snowpack integrity, makes subsequent surveys not fully representative of natural conditions. Recently
developed drone-based systems provides non-invasive and large-scale monitoring of snow cover properties (Bühler et al.,
2016b). To our knowledge, there has been very little research to date using drone-based radar measurement for snow
105 property monitoring (Jenssen and Jacobsen, 2020).

The present study aims to monitor the spatiotemporal variability in h, ρ, *SWE* and *LWC* of a snowpack over flat and sloped
area with a non-destructive approach. This objective is achieved by developing and testing an original combination of drone-
based photogrammetry, drone-based GPR and continuous automatic monitoring including TDR, and field measurements.

2 Study site and condition

110 The study region is the experimental watershed (BVE) of Ste-Marthe, located approximately 70 km west of Montréal, in
Quebec, Canada (45.4239°N, 74.2840°W) (Figure 1.a). The main station of the BVE Ste-Marthe is situated at 120 m.a.s.l. in
an approximately 200 m² large forest clearing (Fig 1.b). A distinction is made between two different topography areas of the
clearance, one categorized as flat and the other as sloped (10%). The main station hosts an automatic weather station (AWS)
that measures various hydroclimatic variables. All data were recorded using a CR1000 data logger (Campbell Scientific).
115 Monitored variables used for the purpose of this study are presented in Table 1. The snowpack outflow at the snow/ground
interface was measured thanks to a custom-built 2.25 m² snow lysimeter.

The frozen ground depth was estimated by interpolation of ground temperatures measured at thermometers buried in the
ground from -10 to -60 cm at 10 cm depth intervals. To avoid interpreting snowpack temperature data that could have been
influenced by solar radiation or by contact with air, snowpack temperature measurements are not considered after March 17,
120 2021, the day the snow height decreased below 40 cm.

Measurements used in this study took place during winter, from February 26, 2021 to March 26, 2021. Two rain-on-snow
(ROS) events occurred during this period. The first ROS was observed from February 28 to March 1, and the second from
March 9 to 12.

Four drone-based surveys were made during that period on February 26, March 5, March 12 and March 19. Figure 2 presents
125 the AWS measurements of interest over the study period. February 26 is considered as the last survey before the end of the
accumulation period, just before the day of maximum snow depth of the winter (February 27). On that date, the snowpack
was cold (at least between 0 and +30 cm) and had not been affected by any significant ROS or major melt event yet.

Between February 27 and March 5, the date of the second survey, the snowpack was first affected by a mild weather episode
of more than 24 hours ending with a ROS event. This episode warmed up the snowpack to nearly 0°C at all measured depths,
130 generated a substantial outflow at the base of the snowpack and increased both the *SWE* and ρ. Interestingly, the outflow at

the snowpack's base occurred while the measured snowpack temperatures were still negative, suggesting the presence of a preferential flow paths over the flat area. The mild weather episode was followed by a marked drop in air temperature, marking the start of a seven-day-long cold period. Over this cold period the snowpack temperatures dropped below 0°C, while *SWE* and *ρ* stabilized. Outflow at the snowpack's base stopped 24 hours after the temperature decreased.

135   Prior to the third survey on March 12, there was a four-day long episode of almost uninterrupted above 0°C air temperatures. On March 11 the air temperature reached a maximum of 15°C and a ROS event occurred. It took two days for the warm conditions to warm the snowpack up to 0°C and to generate outflow at the snowpack's base. The timing and amplitude of the outflow suggest a more homogeneous flow path was present at the time.

March 12 marked the last day of the second mild episode. Snow depth decreased by almost 30%, while *SWE* remained
140   almost unchanged since the last survey, despite substantial liquid precipitations being recorded. Snowpack temperatures and outflow indicate that at least some of the snowpack layers were wet at the time of the survey. At the end of March 12, the air temperature gradually decreased below zero. From that time, air temperatures remained negative until March 17. A freezing front slowly moved down the snowpack, and an interruption of the outflows was observed over that period, suggesting a gradual drying of the snow layers. From March 17 to 19, the dominant warm conditions brought the snowpack temperatures
145   back to the melting point. An outflow of minor amplitude compared to those observed during the two first warm episodes was measured only on March 18. On the March 19 survey, the air temperature dropped down to -2°C.

After March 19, a strong diurnal signal in the outflow marks the start of an uninterrupted loss of mass from the snowpack. Note that over the studied period, at least part of the ground remained frozen, creating a quasi-impermeable barrier to water infiltration (Dingman, 1975).

150   **3 Methods**

The spatiotemporal variability of *h*, *ρ*, *SWE* and *LWC* was assessed by combining different methods with different sampling approaches. Table 2 provides an overview of the different methods used. They are split into three categories, depending on the frequency of measurements and the spatial coverage. Repetitive surveys conducted on the two different areas are used to produce maps of the four studied variables on a weekly basis. Continuous and repetitive measurements at a single point are
155   used as a reference to evaluate the maps accuracy at a given point of the study area. TDR probes represent an exception to that rule. A total of eight probes were split between two spots, one within the flat area and the second within the sloped area. At each spot, probes were placed on different hard layers on the snowpack. These layers were identified as possible vectors for lateral flow (Evans et al., 2016).

3.1 Manual measurements

160   Snow pits were excavated in the flat area following the method presented by Fierz et al. (2009). For each pit, layer identification was followed by a sequential depth, density and snow temperature measurements. Each layer was isolated

from the preceding layer using a thin metallic plate and sampled using a metallic cylinder of 0.3 dm^2 or a cylindrical plastic sampler with a surface of 0.5 dm^2. The sample mass was measured in situ with a precision scale of ±1 g.

Punctual *LWC* measurements were made using an A2 Photonic WISe Sensor (A2) at the snow pit. Two vertical
165 measurement profiles were created for each snow pit. Even if the manufacturer's device precision is ±1% of *LWC*, we anticipate a higher uncertainty, as measurement through ice layers was not possible.

Manual measurements were used to estimate the bulk properties of the snowpack. Bulk *h* and *SWE* were just calculated by summing the individual layer ones. Bulk *ρ* and *LWC* were calculated by taking the weighted mean of the measurements based on layers' length.

3.2 TDR monitoring
170

The CS610 probes were controlled using a TDR200 (both from Campbell Scientific). Each probe was calibrated according to the Campbell Scientific guidelines in the laboratory before deployment. Onsite, each CS610 was left lying over a hard layer without any guide or support. This setup was chosen to allow the probe to move downward together with the supporting hard layer as the snowpack settled. Indeed, maintaining probes at the exact same position above the ground triggers air pocket
175 formation around the metallic rod, affecting the measurements' accuracy (Pérez Díaz et al., 2017). As no visible differences in stratigraphy were observed between the flat and sloped areas over the accumulation period, hard layers supporting the probes were identified the same way:

- *α* represents the ground level. Probes were installed January 8 in the flat area and January 26 at the base of the slope. At both locations, the snow layer on top of the ground was unconsolidated and heterogeneous.
180 - *β* is a wind crust formed December 30–31. Probes were installed the same days as on layer *α*. The layer *β* was overlaid by unconsolidated granular snow.
- *γ* is a hard snow layer formed in mild conditions on January 15. Probes were installed January 26. At that time, the hard snow layer was overlaid by a thin layer of fresh snow.
- *ε* is an ice layer formed during a freezing rain event that occurred February 16. Probes were installed on top of
185 that layer on February 22 in both locations.

TDR probes measured the relative permittivity of the surrounding material. In snow, the relative permittivity is a function of the density and the liquid water content (Stacheder et al., 2009). With a 15-minute measurement interval, it was assumed that noticeable variations in permittivity between two measurements were due to changes in liquid water content, and that changes in density occurred over a longer timescale.

3.3 Drone-based photogrammetry
190

A Mavic 2 Pro UAV (DJI) was used to capture the RGB images used for photogrammetry. The Mavic 2 Pro was upgraded using a global navigation satellite system (GNSS) kit (TopoDrone) to use Post Processed Kinematic (PPK) to correct images' location. The uncertainty claimed by the manufacturer is 3–5 cm in all directions. Corrections were made using a

RS2 (Reach) GNSS base station, with a manufacturer's uncertainty of 4 mm in the horizontal direction and 8 mm in the
195   vertical. After each site visit, collected images were processed using the photogrammetry software Pix4Dmapper (Pix4D) to
produce digital surface models (DSMs). Ground control points, geo-localized using a 7700B GNSS rover (KlauGeomatic),
were used for DSM validation and provide a 3–5 cm uncertainty. Finally, validated DSMs were evaluated and quantified
using the Geographic Information System (GIS) software ArcGIS (ESRI). Following the protocol presented by Bühler et al.
(2016a) and used by Yildiz et al. (2021), the GIS data was used to subtract a snow-free DSM produced on April 6, just after
200   the complete thaw of the snow cover, from the DSM made using images taken over the winter. The final error of the drone
photogrammetry is estimated at ±5 cm.

3.4 Drone-based GPR permittivity measurement

GPR surveys were performed using a Zond 1.5 GHz (Radar System Inc.) carried by a Matrice (M) 600 Pro drone (DJI). GPR
integration and the flight control software (UGCS) were supplied by SPH Engineering. Maximizing GPR measurements
205   requires flying at approximately 1 m above the surveyed surface, managed using a terrain-following system also supplied by
SPH Engineering. The M600 was equipped with a 7700B GNSS (KlauGeomatic) allowing position correction via Post
Processed Kinematic (PPK). Similar to the photogrammetry, corrections were made using the RS2 (Reach) GNSS base
station. Surveys were performed over both the flat and sloped areas. Radargrams' post-treatment was made with the Prism2
software (Radar System Inc.). The GPR system was sampled every 512 ns over both flat and sloped areas, and the drone's
210   flight following north-south transects. For each survey, six transects on the flat area and nine transects on the slope were
surveyed. The distance between two consecutive transects was 50 ± 10 cm. Post-treatment consisted of applying a
background removal filter, adjusting the gain, and applying a time delay compensation. The ground/snow and snow/air
interfaces were detected automatically wherever possible and manually where the layer boundaries were not recognized by
the algorithm. The overall uncertainty for radargram georeferencing is considered to be the same as for photogrammetry.
215   The velocity of the electronic wave within the snowpack (v) and the snow height (h) extracted from the DSM are related as
follows:

$$v = \frac{h}{TWT/2},$$ (1)

where TWT is the two-way travel time of the wave within the snowpack in ns. TWT is extracted from the radargrams by
taking the difference between the air/snow interface and snow/ground interface two-way travel times.
220   The relative permittivity of the snowpack is a complex number. Its real part (ε_s') is calculated using Neal (2004)

$$\varepsilon_s' = (v/c)^2,$$ (2)

where c stands for the velocity of light in a vacuum (taken as equal to 0.3 m/ns).

3.5 Drone-based GPR frequency-dependent attenuation analysis

In wet conditions, the imaginary part of the permittivity of the snow (ε_s'') is estimated using the GPR frequency-dependent attenuation analysis method proposed by Bradford et al. (2009). In the standard GPR frequency range (10 MHz–1 GHz), ε_s' is strongly dependent on *LWC* and assumed to be independent of frequency. Assuming that the frequency-dependent attenuation of an electromagnetic wave through water is linearly related to frequency (Turner and Siggins, 1994), the attenuation coefficient over the GPR signal band can be written as

$$\alpha = \alpha_0 + \frac{\sqrt{\mu_0 \varepsilon_s'}}{2Q^*}\omega,$$
(3)

Where Q^* representing the generalization of the attenuation quality parameter in the linear region of the attenuation, α_0 the impact of low frequencies in the radar attenuation, and μ_0 the permeability in the free space.

Within the frequency range of 1 to 1500 MHz, Q^* is assumed to be constant (Bradford et al., 2009) and related to ε_s'' as follows:

$$Q^* = \frac{\varepsilon_s'}{2\varepsilon_s''},$$
(4)

Where a GPR generates waves in the form of a Ricker wavelet, the frequency f_0 of the spectral maximum of the GPR wave measured at the snow/air interface on the radargram and the frequency f_t of the spectral maximum measured at the ground/snow interface are related to Q^* (Bradford, 2007):

$$\begin{cases} \frac{1}{Q^*} = \frac{4}{TWT}\frac{\omega_0^2 - \omega_t^2}{\omega_0^2 \omega_t} \\ \omega_0 = 2\pi f_0 \\ \omega_t = 2\pi f_t \end{cases},$$
(5)

f_0 and f_t were measured by randomly sampling at least 10 points for each GPR line. For each selected point, readings were made on five consecutive traces using the Prism2 software. Peak frequencies for each point were calculated by taking the median of the measurements. When at least one trace showed a higher frequency at the ground/snow interface than at the snow/air interface, two extra traces were used; ε_s'' was then computed using equations (4) and (5), with ε_s' being calculated using equation (2).

LWC and the relative density of dry snow (ρ_d) were then calculated with the following set of empirical equations proposed by Tiuri et al. (1984) and Sihvola and Tiuri (1986):

$$\varepsilon_d' = (1 + 1.7\rho_d + 0.7\rho_d^2),$$
(6)

$$\varepsilon_s' = (0.1LWC + 0.8LWC)\varepsilon_w' + \varepsilon_d',$$
(7)

$$\varepsilon_s'' = (0.1LWC + 0.8LWC)\varepsilon_w'',$$
(8)

where ε_d' is the bulk permittivity of dry snow and ε_w' and ε_w'' are respectively the real and the imaginary parts of the relative

250   permittivity of pure water.

Equations 2.6, 2.7, and 2.8 were established for a measurement frequency of 1 GHz and are assumed to remain valid for the purpose of the present study.

The relative snow density (ρ) is then calculated with the following equation:

$$\rho = \rho_d + LWC, \tag{9}$$

255   Finally, the *SWE* is calculated using the *h* extracted from the DSM produced by photogrammetry:

$$SWE = h.\rho, \tag{10}$$

LWC maps were then produced by extrapolating the punctual results to areas value using a Kernel algorithm with the Geostatistical Wizard module of the ArcGIS software.

For the surveys on February 26 and March 5, the snowpack was assumed to be dry, as the survey was preceded by several

260   cold days with a snowpack temperature below 0°C. The *SWE* was determined using the assumptions that $\varepsilon_d'=\varepsilon_s'$, $\rho_s=\rho_d$, and *LWC*=0.

For the surveys on March 12 and March 19, the *SWE* was determined following the GPR attenuation analysis.

4 Results

4.1 Drone-based photogrammetry

265   None of the control points used in each survey showed significant difference with the PPK-based DSM produced by photogrammetry, validating the method for the purpose of this study. Further, the adjustments made at the final stage of the DSM production, when ground control points were compared with PPK-based points, were all under 3 cm, which is within the expected accuracy of the PPK devices.

Maps of snow depth obtained from the photogrammetry are presented in Figure 3.

270   The individual maps make visually accurate representations of the study site. Prints of the paths we used over the entire season (e.g., lines in yellow on the 26/02 map) show consistent reductions in snow depth compared to pristine areas. Similarly, extra snow accumulation in drainage ditches (e.g., brown area in the bottom left area of the 19/03 map) is well marked and consistent between the survey dates. Overall, those maps are considered as satisfactory for the purpose of the study.

275   By comparing the different survey dates, we observe that the snow depth decrease that occurred between February 26 and March 5 appears to be homogeneous over the entire area, with no differences between the flat and sloped areas being visually noticeable. This is not the case when comparing the March 12 map to the two first dates. The severe ablation and/or settling that affected the study area impacted the sloped area more than the flat one. Changes in snow depth were less

pronounced between March 12 and 19 than for the previous period. However, the difference between the flat and sloped
280   areas remained important.

Overall, Figure 3 shows that the sloped and flat sections had comparable snow depths during the accumulation period but
reacted differently at the start of the ablation period, with a faster loss of height in the sloped area than in the flat one.

4.2 TDR monitoring

TDR measurements of the snow's relative permittivity were normalized to the February 26 at 12:30 values to allow
285   comparison between the different layers, areas and times (Figure 4). As described in the Methods Section, fast variations in
relative permittivity are associated with a change in *LWC*. Timewise, we observe that the first mild episode, starting
February 27, generated a tiny increase in *LWC* above the upper hard layer a day after it started. Interestingly, the lysimeter
measured outflow at the base of the snowpack in the flat area 24 hours before any moisture increase was detected by the
TDR probe placed on the ground in the flat area. Snowpack response to the February 28 ROS event occurred first at the
290   bottom of the sloped area, followed by a limited increase in snow moisture above the hard snow layers. Detection of an
increase in *LWC* at the base of the flat area occurred half a day after the increase for the sloped area, at a time that the air
temperature had already dropped below zero. Past that time, normalized permittivity at all spots steadily decreased, reaching
a plateau representative of the new dry densities of the snow layers. Differences observed in timing and amplitudes at the
different probe locations suggest that liquid water flows followed preferential pathways, confirming what was assumed from
295   *AWS* measurements. The *LWC* increased in response to the second mild episode, first at the base of the sloped area too. The
increase was followed by an increase at the other probes 24 hours later, those above the β and γ layers being of very low
amplitude. As was the case during the first mild episode, the strongest increase in *LWC* was measured over the sloped
ground. At the end of the 10th of March, three of the four probed layers showed an increase in *LWC*, which was more
pronounced in the sloped area than in the flat area. After March 10, in the sloped area the fluctuation of *LWC* above the γ
300   layers started to mimic the one aboveground, but with a lower amplitude. This synchronism suggests that the sloped area's
preferential pathway flow-through mode started weakening. The sloped area showed a faster and more intense response to
the mild episode starting March 17 compared to the flat area too. Unlike the flat area, the slope's *LWC* fluctuation started
exhibiting a strong diurnal pattern, whose peak occurred a couple of hours before the peak in air temperature and the peak in
lysimeter outflow. This suggests the slope was more responsive to the incoming solar radiation compared to the flat area.
305   Overall, the TDR probes showed a faster and more intense response to mild warming episodes on the slope compared to the
flat area, the presence of preferential pathways (particularly at the start of the ablation period), and a noticeably higher
influence of solar radiation on the ablations of the sloped area compared to the flat one at the end of the study period.

4.3 Drone-based GPR permittivity measurement

For each survey day, each area, *h* was extracted from the DSM following the north-to-south transects covered by the M600
310   pro during the GPR survey. Snow depth and snowpack bulk permittivity profiles of selected transects are shown in Figure 5.

On February 26, the flat area shows quite stable bulk permittivity and snow depth profiles. The slope transect exhibits slightly lower snow depth and higher bulk permittivity than the sloped section. The bulk permittivity over the sloped section appears more variable than the flat one too. The March 5 show limited changes compared to the 26th of February for both variables and both areas.

315 The March 12 transects show a sharp change compared to the two first dates. Both areas exhibited a rise in bulk permittivity and a decrease in snow depth. Bulk permittivity profiles show gaps due to the GPR signal not penetrating fully through the wet snow. Ranging from 0.41 to 0.78, the sloped area bulk permittivity variability is more pronounced than of the flat area. On March 19, the snow depth in the flat transects remained almost similar to that measured on March 12. The bulk permittivity decreased to values situated between those of March 5 and 12. The sloped area transect exhibited a decrease in

320 bulk permittivity, like that of the flat area transect, and its variability remained higher than in the flat section. On March 19, the main difference between the two sections was the snow depth. The sloped area showed a more pronounced decrease than the flat area. As no fresh precipitations were recorded between March 12 and 19, the decrease in permittivity in both sections can be interpreted as a decrease in *LWC*, which could have occurred together with snow densification in the sloped section.

Overall, Figure 5 confirms the difference in response to the mild event of March 11 between the sloped area and the flat area,

325 including a high moisture content for both areas and a more pronounced densification of the snowpack over the sloped area compared to the flat area.

4.3 Drone-based GPR frequency-dependent attenuation analysis

Results from the *LWC* calculation and interpolation are presented in Figure 6.

Contradicting snow temperature profiles and A2 measurements, Figure 6 suggests the February 26 and March 5 snowpacks

330 present *LWC* ranging from 0 to 3% with no visible differentiation between the sloped and flat areas. Both dates show a relative spatial heterogeneity in *LWC* with no clear common patterns between the two dates.

The March 12 survey shows a general increase in *LWC* compared with the two previous surveys, and a differentiation between the two studied areas. The slope area exhibits the highest overall LWC, although both areas are spatially variable.

Compared to March 12, the *LWC* map for March 19 has lower values in the sloped area compared to the flat area, making

335 both areas difficult to differentiate. *LWC* values remains highly variable for both sections.

Overall, Figure 6 confirms that, unlike the ROS event that occurred at the end of February, the sloped and flat areas responded in different ways to the March 11 ROS event. On the other hand, *LWC* non-null values seem unrealistic for the two first survey dates that followed the pronounced cold episode. In a similar way, the absence of a recurrent spatial pattern in *LWC* variations between maps of different dates suggests the method was not able to capture these variations in a detailed

340 way.

5 Discussion

Drone-based estimation of key snowpack variables

In the present study, the spatiotemporal variability in h, ρ, SWE and LWC, four key proprieties of a snowpack, has been assessed using drone-based GPR and photogrammetry methods in a repetitive way. Figure 7 provides an overview of the variability in a form of boxplots and, where possible, compares drone-based measurements to those of the AWS and from snow pits.

Photogrammetry results are in good agreement with those of the AWS and of the snow pits over the entire study period, with a possible slight overestimation in the two first surveys. Snow depth over the flat area consistently shows a narrow distribution. The slope is characterized by a lower snow depth and a larger variability than the flat, especially after the ROS event that occurred on March 11.

The LWC boxplots in Figure 7 represent well the general evolution of the snowpack moisture content through time: a stable situation occurring between the first two survey dates, followed by a marked increase in snow moisture on March 12 and a slight decrease on March 19 (for the sloped area only). The boxplot also captures the difference in response to mild events between the flat and sloped areas. Compared to the A2 measurements, the boxplots show the method is not able to provide realistic LWC absolute values. Even if we consider that the A2 measurements did not sample the entire snow column and therefore might have underestimated the snowpack average LWC, the drone-based result appears by far overestimated.

Although less obvious than for the LWC, ρ estimation appear to diverge from the reference measurements also. The drone-based method underestimates ρ over the flat area compared with both the AWS and the snow pit measurements for the first two and the last dates, while overestimating it for March 12. Moreover, both the flat and sloped areas exhibit an unrealistic 50% decrease in ρ between March 12 and 18, as no fresh snowfall occurred between those two dates.

Calculated as the product of h by ρ, SWE boxes show similar characteristics to ρ.

Interestingly, we note that while Figure 5 shows the bulk permittivity profile being coherent with TDR and AWS measurements, this was not the case anymore in the computed variables presented in Figure 7. As described earlier, the bulk permittivity of the snowpack is influenced by both ρ and LWC. Figure 7 therefore suggests that the method we applied failed to differentiate the relative influence of both variables.

Our method makes use of empirical Equations (6), (7) and (8), which are commonly used in snow hydrology. According to Tiuri et al. (1984), Equations (7) and (8) are valid in pendular regime, for $\varepsilon_s' \leq 2.6$ ($\varepsilon_s' \leq 3$ for Colbeck (1982)), as opposed to a funicular regime. In a layered snowpack in which preferential flow occurs, it is realistic to hypothesize that both regimes occur in the snow column, making Equations (7) and (8) possibly not directly applicable to bulk relative permittivity measurements.

Different empirical formulas relating the relative permittivity to ρ have been subsequently developed (e.g. Di Paolo et al. (2018); Frolov and Macheret (1999)). In the present study, we decided to use the formulas presented in Tiuri et al. (1984) as they are most commonly used in the literature. Assessing the other formulas might be a way to improve the absolute values

of key snowpack variables. As suggested by Webb et al. (2021), re-assessing the application conditions of the equation used in the present study is probably required.

Fixing the relative density of the snow based on manual sampling or AWS values could represent another solution to the problem met in differentiating between the relative influence of ρ and *LWC* on bulk permittivity. However, this solution would not allow for the capturing of the spatial variability in ρ and therefore might bias calculations.

Spatiotemporal variability in snowpack characteristics

TDR monitoring, drone-based photogrammetry and drone-based GPR have been shown to make a valuable combination for assessing the spatiotemporal variability in key snowpack variables. The use of photogrammetry to map snow depth over the study area has given the opportunity to calculate bulk permittivity from repetitive drone-based GPR surveys. Both bulk permittivity and snow depth profiles agreed with site observations and reference measurements. Converting the bulk permittivity into absolute ρ, *LWC* and *SWE* values do not provide the expected results even if the temporal evolution of those parameters was captured in an acceptable way. TDR monitoring complemented the drone-based measurements, providing both high temporal resolution and layer-based snowpack relative permittivity time series. Except for the ρ, *LWC* and *SWE* calculations, the different methods were highly consistent compared to each other, allowing for the capture of the flat and sloped areas responses to changes in meteorological conditions.

More precisely, the results obtained in this study show that:

- The flat and sloped areas had comparable responses to the first ROS event of the study period, which occurred at the end of February. That event produced snowpack outflows and increases in *LWC*, especially at the base of both areas. The sloped area, however, showed a faster and more intense response than the flat one.
- The first ROS episode did not modify the snowpack's ρ and h profiles in a substantial way. Both study areas exhibited characteristics of preferential flow pathways.
- The second ROS event that occurred on March 10 affected the sloped area in a different way than the flat one, both areas showing important differences in h, *LWC* and ρ in the March 12 surveys.
- The third mild episode that occurred from March 16 to 18 did not drastically modify the characteristics of both areas compared to the March 12 situation. However, the slope showed faster rates of melt/ablation, probably due to its southward orientation.

6 Conclusion

A combination of TDR monitoring, drone-based photogrammetry and drone-based GPR was used in the experimental watershed of Ste-Marthe (Quebec, Canada) over the winter of 2020–2021. The suite of methods showed comparable snow accumulation over flat and sloped areas, with comparable characteristics lasting after the first ROS event. The second ROS event at the start of the ablation season led to differences in response between the two areas.

Drone-based GPR was very instructive when interpretation was based on bulk permittivity results but showed limitations for mapping ρ, *SWE* and *LWC*. There are questions about the applicability of empirical equations used given the site conditions. The results suggest the empirical equations should be reassessed for conditions that differ from the ones they were formulated for. The method did not allow getting the full benefit from applying the GPR frequency dependant attenuation

410   method to estimate *LWC* in snowpack. The method however shows promise. In the 2020-2021 winter, the radargram obtained using a 1.5 GHz GPR was not detailed enough to differentiate between the main snowpack layers. However, efforts should be continued in this regard, as the 2020–2021 snowpack was characterized by a relatively low snow depth and an uneven disposition of the ice layers in the snow column.

Autor contributions

415   MB, ER and FB framed the research project, fixed the objectives and made the research project steering group. EV designed the research and organized the fieldwork. EV and MB collected data in the field. CM conducted a substantial part of the GPR data treatment. EV produced all the other results and made the interpretation. EV Wrote the initial draft of the paper. All authors contributed to editing and revising the paper.

Code/Data availability

420   The data are available on request to the corresponding author.

Competing interests

The authors declare that they have no conflict of interest.

Acknoledgment

This research is supported by the Geochemistry and Geodynamics Research Centre (Geotop) of Quebec, the Quebec Water
425   Research Center (Centreau), FRQNT and the Natural Sciences and Engineering Research Council of Canada (NSERC), and the Ecole de Technologie Superieure, a member of the Université du Quebec. The authors are grateful for the invaluable support from the municipality of Sainte-Marthe, Quebec, Canada.

References

430 Andradóttir, H. Ó., Arnardóttir, A. R., and Zaqout, T.: Rain on snow induced urban floods in cold maritime climate: Risk, indicators and trends, Hydrological Processes, 35, e14298, https://doi.org/10.1002/hyp.14298, 2021.

Bradford, J. H.: Frequency-Dependent Attenuation Analysis of Ground-Penetrating Radar Data, John H. Bradford, 72, 10.1190/1.2710183, 2007.

Bradford, J. H., Harper, J. T., and Brown, J.: Complex dielectric permittivity measurements from ground-penetrating radar
435 data to estimate snow liquid water content in the pendular regime, Water Resources Research, 45, 10.1029/2008wr007341, 2009.

Brown, R., Tapsoba, D., and Derksen, C.: Evaluation of snow water equivalent datasets over the Saint-Maurice river basin region of southern Québec, Hydrological Processes, 32, 2748-2764, 10.1002/hyp.13221, 2018.

Bühler, Y., Adams, M., Bösch, R., and Stoffel, A.: Mapping snow depth in alpine terrain with unmanned aerial systems
440 (UAS): potential and limitations, The Cryosphere Discussions, 10.5194/tc-2015-220, 2016a.

Bühler, Y., Stoffel, A., Adams, M., Bösch, R., and Ginzler, C.: UAS Photogrammetry of Homogenous Snow Cover, 2016b.

Chen, P., Li, Z., and Zheng, N.: A New Approach for GNSS-IR Snow Depth Monitoring With Slope Correction and Error Prediction, 10.21203/rs.3.rs-150402/v1, 2021.

Colbeck, S. C.: The geometry and permittivity of snow at high frequencies, Journal of Applied Physics, 53, 4495-4500,
445 10.1063/1.331186, 1982.

Conger, S. M. and McClung, D. M.: Comparison of density cutters for snow profile observations, Journal of Glaciology, 55, 163-169, 10.3189/002214309788609038, 2009.

Deems, J. S., Painter, T. H., and Finnegan, D. C.: Lidar measurement of snow depth: a review, Journal of Glaciology, 59, 467-479, 10.3189/2013JoG12J154, 2017.

450 Denoth, A.: An electron device for long-term snow wetness recording, International Journal of Rock Mechanics and Mining Sciences and Geomechanics Abstracts, 32, 144A-145A, 10.1016/0148-9062(95)90311-R, 1995.

DeWalle, D. R. and Rango, A.: Principles of Snow Hydrology, Cambridge University Press2008.

Di Paolo, F., Cosciotti, B., Lauro, S., Mattei, E., and Pettinelli, E.: Dry snow permittivity evaluation from density: A critical review, 1-5 pp., 10.1109/ICGPR.2018.8441610, 2018.

455 Dierauer, J. R., Allen, D. M., and Whitfield, P. H.: Climate change impacts on snow and streamflow drought regimes in four ecoregions of British Columbia, Canadian Water Resources Journal / Revue canadienne des ressources hydriques, 46, 168-193, 10.1080/07011784.2021.1960894, 2021.

Ding, Y., Mu, C., Wu, T., Hu, G., Zou, D., Wang, D., Li, W., and Wu, X.: Increasing cryospheric hazards in a warming climate, Earth-Science Reviews, 213, 103500, https://doi.org/10.1016/j.earscirev.2020.103500, 2021.

460 Dingman, S.: Hydrologic Effects of Frozen Ground: Literature Review and Synthesis, 60, 1975.

Doesken, N. J., Ryan, W. A., and Fassnacht, S. R.: Evaluation of Ultrasonic Snow Depth Sensors for U.S. Snow Measurements, Journal of Atmospheric and Oceanic Technology, 25, 667-684, 10.1175/2007jtecha947.1, 2008.

Evans, S. L., Flores, A. N., Heilig, A., Kohn, M. J., Marshall, H. P., and McNamara, J. P.: Isotopic evidence for lateral flow and diffusive transport, but not sublimation, in a sloped seasonal snowpack, Idaho, USA, Geophysical Research Letters, 43,
465 3298-3306, 10.1002/2015gl067605, 2016.

Fierz, C., R.L, A., Y, D., P, E., Greene, E., McClung, D., Nishimura, K., Satyawali, P., and Sokratov, S.: The international classification for seasonal snow on the ground (UNESCO, IHP (International Hydrological Programme)–VII, Technical Documents in Hydrology, No 83; IACS (International Association of Cryospheric Sciences) contribution No 1), 2009.

Ford, C. M., Kendall, A. D., and Hyndman, D. W.: Snowpacks decrease and streamflows shift across the eastern US as
470 winters warm, Science of The Total Environment, 793, 148483, https://doi.org/10.1016/j.scitotenv.2021.148483, 2021.

Foster, J., Sun, C., Walker, J., Kelly, R., Chang, A., Dong, J., and Powell, H.: Quantifying the uncertainty in passive microwave snow water equivalent observations, Remote Sensing of Environment, 94, 187-203, 10.1016/j.rse.2004.09.012, 2005.

Frolov, A. D. and Macheret, Y.: On dielectric properties of dry and wet snow, Hydrological Processes, 13, 1755-1760,
475 10.1002/(SICI)1099-1085(199909)13:12/13<1755::AID-HYP854>3.0.CO;2-T, 1999.

Gergel, D. R., Nijssen, B., Abatzoglou, J. T., Lettenmaier, D. P., and Stumbaugh, M. R.: Effects of climate change on snowpack and fire potential in the western USA, Climatic Change, 141, 287-299, 10.1007/s10584-017-1899-y, 2017.

Gergely, M., Schneebeli, M., and Roth, K.: First experiments to determine snow density from diffuse near-infrared transmittance, Cold Regions Science and Technology, 64, 81-86, 10.1016/j.coldregions.2010.06.005, 2010.

480 Godio, A., Frigo, B., Chiaia, B., Maggioni, P., Freppaz, M., Ceaglio, E., and Dellavedova, P.: Integration of upward GPR and water content reflectometry to monitor snow properties, Near Surface Geophysics, 16, 154-163, 10.3997/1873-0604.2017060, 2018.

Goodison, B. E., Glynn, J. E., Harvey, K. D., and Slater, J. E.: Snow Surveying in Canada: A Perspective, Canadian Water Resources Journal, 12, 27-42, 10.4296/cwrj1202027, 1987.

485 Hao, J., Mind'je, R., Feng, T., and Li, L.: Performance of snow density measurement systems in snow stratigraphies, Hydrology Research, 52, 834-846, 10.2166/nh.2021.133, 2021.

Harder, P., Pomeroy, J., and Helgason, W.: Improving sub-canopy snow depth mapping with unmanned aerial vehicles: lidar versus structure-from-motion techniques, The Cryosphere, 14, 1919-1935, 10.5194/tc-14-1919-2020, 2020.

Hawley, R., Brandt, O., Morris, E., Kohler, J., Shepherd, A., and Wingham, D.: Instruments and Methods Techniques for
490 measuring high-resolution firn density profiles: case study from Kongsvegen, Svalbard, Journal of Glaciology, 54, 463-468, 10.3189/002214308785837020, 2008.

Hodgkins, G. A. and Dudley, R. W.: Changes in late-winter snowpack depth, water equivalent, and density in Maine, 1926–2004, Hydrological Processes, 20, 741-751, https://doi.org/10.1002/hyp.6111, 2006.

Jenssen, R. O. R. and Jacobsen, S.: Drone-mounted UWB snow radar: technical improvements and field results, Journal of
495 Electromagnetic Waves and Applications, 34, 1930-1954, 10.1080/09205071.2020.1799871, 2020.

Kinar, N. and Pomeroy, J.: SAS2: the system for acoustic sensing of snow: SAS2: The System for Acoustic Sensing of Snow, Hydrological Processes, 29, 10.1002/hyp.10535, 2015a.

Kinar, N. and Pomeroy, J.: Measurement of the physical properties of the snowpack, Reviews of Geophysics, 53, 481-544, 10.1002/2015rg000481, 2015b.

500 Koutantou, K., Mazzotti, G., and Brunner, P.: Uav-Based Lidar High-Resolution Snow Depth Mapping in the Swiss Alps: Comparing Flat and Steep Forests, The International Archives of the Photogrammetry, Remote Sensing and Spatial Information Sciences, XLIII-B3-2021, 477-484, 10.5194/isprs-archives-XLIII-B3-2021-477-2021, 2021.

Leppänen, L., Kontu, A., Hannula, H.-R., Sjöblom, H., and Pulliainen, J.: Sodankylä manual snow survey program, Geoscientific Instrumentation, Methods and Data Systems, 5, 163-179, 10.5194/gi-5-163-2016, 2016.

505 Li, D., Lettenmaier, D. P., Margulis, S. A., and Andreadis, K.: The Role of Rain-on-Snow in Flooding Over the Conterminous United States, Water Resources Research, 55, 8492-8513, 10.1029/2019wr024950, 2019.

Lindström, G., Pers, C., Rosberg, J., Strömqvist, J., and Arheimer, B.: Development and testing of the HYPE (Hydrological Predictions for the Environment) water quality model for different spatial scales, Hydrology Research, 41, 295-319, 10.2166/nh.2010.007, 2010.

510 Liu, J. and Lobb, D. A.: An Overview of Crop and Crop Residue Management Impacts on Crop Water Use and Runoff in the Canadian Prairies, Water, 13, 10.3390/w13202929, 2021.

Lundberg, A., Kruglyak, A., Gustafsson, D., and Sundström, N.: Field evaluation of a new method for estimation of liquid water content and snow water equivalent of wet snowpacks with GPR, Hydrology Research, 44, 600-613, 10.2166/nh.2012.182, 2013.

515 Lundberg, A., Gustafsson, D., Stumpp, C., Klöve, B., and Feiccabrino, J.: Spatiotemporal Variations in Snow and Soil Frost—A Review of Measurement Techniques, Hydrology, 3, 28, 10.3390/hydrology3030028, 2016.

Magnusson, J., Jonas, T., López-Moreno, I., and Lehning, M.: Snow cover response to climate change in a high alpine and half-glacierized basin in Switzerland, Hydrology Research, 41, 230-240, 10.2166/nh.2010.115, 2010.

Mas, A., Baraer, M., Arsenault, R., Poulin, A., and Préfontaine, J.: Targeting high robustness in snowpack modeling for
520 Nordic hydrological applications in limited data conditions, Journal of Hydrology, 564, 1008-1021, https://doi.org/10.1016/j.jhydrol.2018.07.071, 2018.

Mavrovic, A., Madore, J.-B., Langlois, A., Royer, A., and Roy, A.: Snow liquid water content measurement using an open-ended coaxial probe (OECP), Cold Regions Science and Technology, 171, 10.1016/j.coldregions.2019.102958, 2020.

Morris, E. and Cooper, J.: Instruments and Methods Density measurements in ice boreholes using neutron scattering, Journal
525 of Glaciology, 49, 599-604, 10.3189/172756503781830403, 2003.

Morse, B. and Turcotte, B.: Risque d'inondations par embâcles de glaces et estimations des débits hivernaux dans un contexte de changements climatiques, Rapport présenté à Ouranos, 2018.

Mortimer, C., Mudryk, L., Derksen, C., Luojus, K., Brown, R., Kelly, R., and Tedesco, M.: Evaluation of long-term Northern Hemisphere snow water equivalent products, The Cryosphere, 14, 1579-1594, 10.5194/tc-14-1579-2020, 2020.

530   Najafi, M. R., Zwiers, F., and Gillett, N.: Attribution of the Observed Spring Snowpack Decline in British Columbia to Anthropogenic Climate Change, Journal of Climate, 30, 4113-4130, 10.1175/jcli-d-16-0189.1, 2017.

Neal, A.: Ground-penetrating radar and its use in sedimentology: Principles, problems and progress, Earth-Science Reviews, 66, 261-330, 10.1016/j.earscirev.2004.01.004, 2004.

Paquotte, A. and Baraer, M.: Hydrological behaviour of an ice-layered snowpack in a non-mountainous environment,
535   Hydrological Processes, 36, 10.1002/hyp.14433, 2022.

Pérez Díaz, C. L., Muñoz, J., Lakhankar, T., Khanbilvardi, R., and Romanov, P.: Proof of Concept: Development of Snow Liquid Water Content Profiler Using CS650 Reflectometers at Caribou, ME, USA, Sensors, 17, 647, 2017.

Previati, M., Godio, A., and Ferraris, S.: Validation of spatial variability of snowpack thickness and density obtained with GPR and TDR methods, Journal of Applied Geophysics, 75, 284-293, 10.1016/j.jappgeo.2011.07.007, 2011.

540   Prokop, A.: Assessing the applicability of terrestrial laser scanning for spatial snow depth measurements, Cold Regions Science and Technology, 54, 155-163, 10.1016/j.coldregions.2008.07.002, 2008.

Quéno, L., Fierz, C., van Herwijnen, A., Longridge, D., and Wever, N.: Deep ice layer formation in an alpine snowpack: monitoring and modeling, The Cryosphere, 14, 3449-3464, 10.5194/tc-14-3449-2020, 2020.

Revuelto, J., López-Moreno, J. I., Azorin-Molina, C., and Vicente-Serrano, S. M.: Canopy influence on snow depth
545   distribution in a pine stand determined from terrestrial laser data, Water Resources Research, 51, 3476-3489, 10.1002/2014wr016496, 2015.

Rott, H., Nagler, T., and Scheiber, R.: Snow mass retrieval by means of SAR interferometry, 2003.

Royer, A., Roy, A., Jutras, S., and Langlois, A.: Review article: Performance assessment of radiation-based field sensors for monitoring the water equivalent of snow cover (SWE), The Cryosphere, 15, 5079-5098, 10.5194/tc-15-5079-2021, 2021.

550   Sihvola, A. and Tiuri, M.: Snow Fork for Field Determination of the Density and Wetness Profiles of a Snow Pack, Geoscience and Remote Sensing, IEEE Transactions on, 24, 717-721, 10.1109/TGRS.1986.289619, 1986.

Stacheder, M., Koeniger, F., and Schuhmann, R.: New Dielectric Sensors and Sensing Techniques for Soil and Snow Moisture Measurements, Sensors, 9, 2951-2967, 2009.

Sturm, M. and Holmgren, J.: An Automatic Snow Depth Probe for Field Validation Campaigns, Water Resources Research,
555   54, 9695-9701, https://doi.org/10.1029/2018WR023559, 2018.

Sun, F., Berg, N., Hall, A., Schwartz, M., and Walton, D.: Understanding End-of-Century Snowpack Changes Over California's Sierra Nevada, Geophysical Research Letters, 46, 933-943, https://doi.org/10.1029/2018GL080362, 2019.

Tiuri, M., Sihvola, A., Nyfors, E., and Hallikaiken, M.: The complex dielectric constant of snow at microwave frequencies, IEEE Journal of Oceanic Engineering, 9, 377-382, 10.1109/joe.1984.1145645, 1984.

560   Turner, G. and Siggins, A. F.: Constant Q attenuation of subsurface radar pulses, GEOPHYSICS, 59, 1192-1200, 10.1190/1.1443677, 1994.

E. Valence et M. Baraer. 2021. Impact of the spatial and temporal variability of the snowpack conditions on internal liquid water fluxes. Western Snow Conference Proceeding, June 2021.

Vionnet, V., Mortimer, C., Brady, M., Arnal, L., and Brown, R.: Canadian historical Snow Water Equivalent dataset
565   (CanSWE, 1928–2020), Earth System Science Data, 13, 4603-4619, 10.5194/essd-13-4603-2021, 2021.

Webb, R. W., Wigmore, O., Jennings, K., Fend, M., and Molotch, N. P.: Hydrologic connectivity at the hillslope scale through intra-snowpack flow paths during snowmelt, Hydrological Processes, 34, 1616-1629, 10.1002/hyp.13686, 2020.

Webb, R. W., Marziliano, A., McGrath, D., Bonnell, R., Meehan, T. G., Vuyovich, C., and Marshall, H.-P.: In Situ Determination of Dry and Wet Snow Permittivity: Improving Equations for Low Frequency Radar Applications, Remote
570   Sensing, 13, 10.3390/rs13224617, 2021.

Yildiz, S., Akyurek, Z., and Binley, A.: Quantifying snow water equivalent using terrestrial ground penetrating radar and unmanned aerial vehicle photogrammetry, Hydrological Processes, 35, 10.1002/hyp.14190, 2021.

Yu, K., Li, Y., Jin, T., Chang, X., Wang, Q., and Li, J.: GNSS-R-Based Snow Water Equivalent Estimation with Empirical Modeling and Enhanced SNR-Based Snow Depth Estimation, Remote Sensing, 12, 10.3390/rs12233905, 2020.

575   Zhang, G., Yao, T., Xie, H., Wang, W., and Yang, W.: An inventory of glacial lakes in the Third Pole region and their changes in response to global warming, Global and Planetary Change, 131, 148-157, https://doi.org/10.1016/j.gloplacha.2015.05.013, 2015.
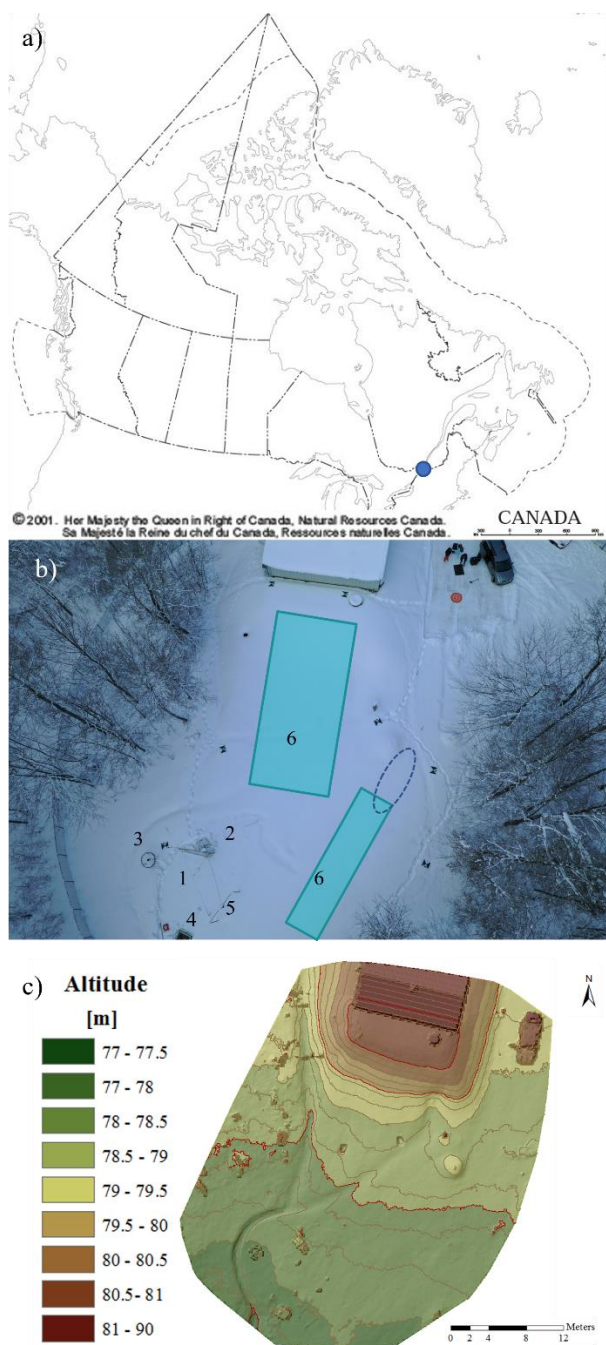
Figure 1: Study Site. a) Location of the BVE Ste-Marthe. b) Overview of the main station; blue areas represent the two studied areas and dashed dark blue ellipse represent the zone used for snow pit. Numbers identify devices of interest for the present study: (1) sonic sensor, (2) ground and snow temperature sensors, (3) shielded precipitation gauge, (4) snow lysimeter, (5) *SWE* sensor and (6) TDRs. c) DSM of the main station area.
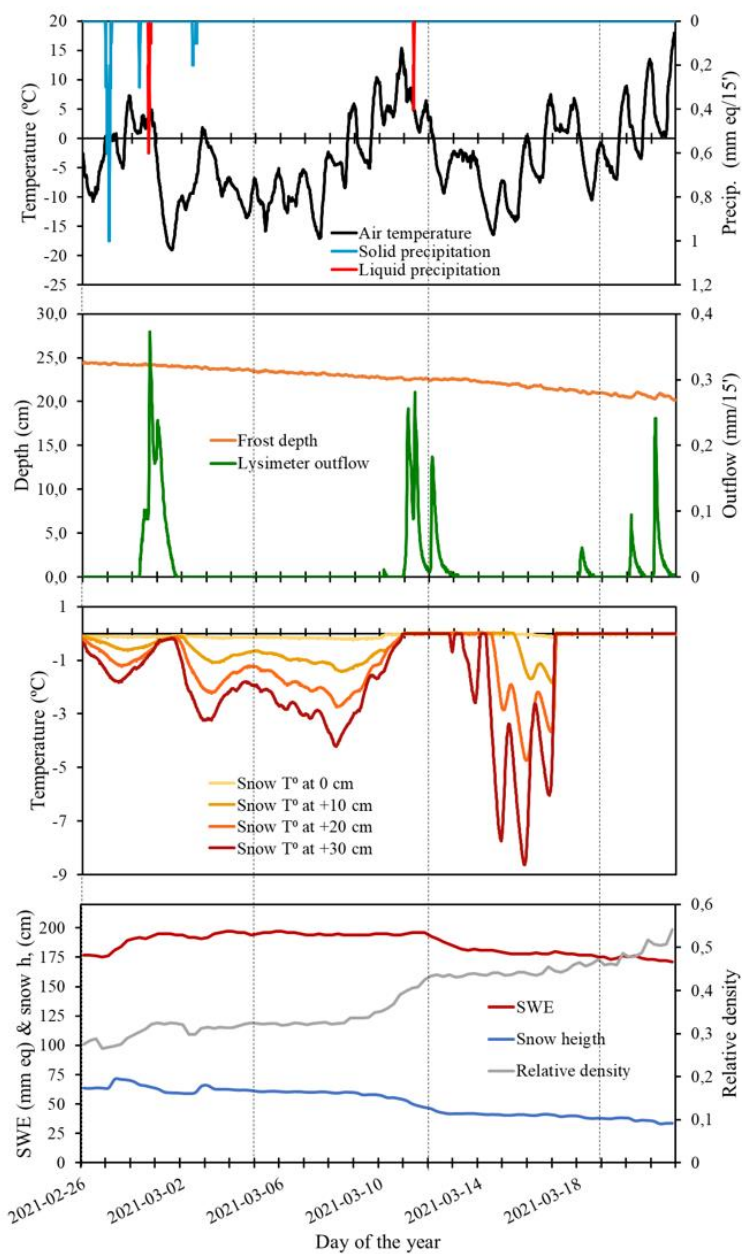
585

Figure 2: AWS measurements during the winter 2022 ablation period. Vertical dashed lines indicate field measurements days. Variables' names are indicated in each subfigure. Details about variables' descriptions and measurements are given in Table 1.

Snow Depth [m]

■	-15 - -0,05
■	-0,05 - 0
■	0 - 0,05
■	0,05 - 0,1
■	0,1 - 0,15
■	0,15 - 0,2
■	0,2 - 0,25
■	0,25 - 0,3
■	0,3 - 0,35
■	0,35 - 0,4
■	0,4 - 0,45
■	0,45 - 0,5
■	0,5 - 0,55
■	0,55 - 0,6
■	0,6 - 0,65
■	0,65 - 0,7
■	0,7 - 0,75
■	0,75 - 0,8
■	0,8 - 0,85
■	0,85 - 0,9
■	0,9 - 0,95
■	0,95 - 15
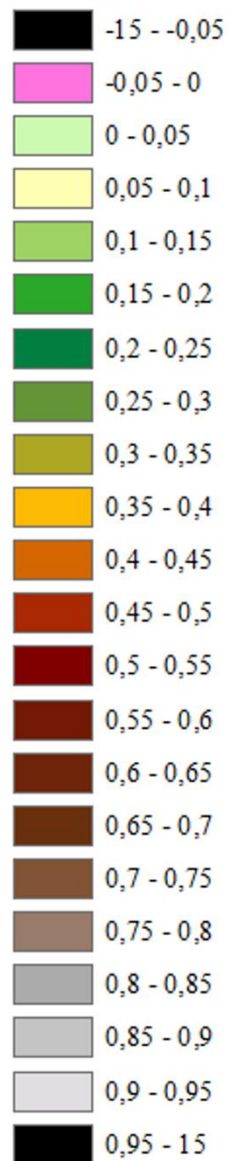
26/02   05/03
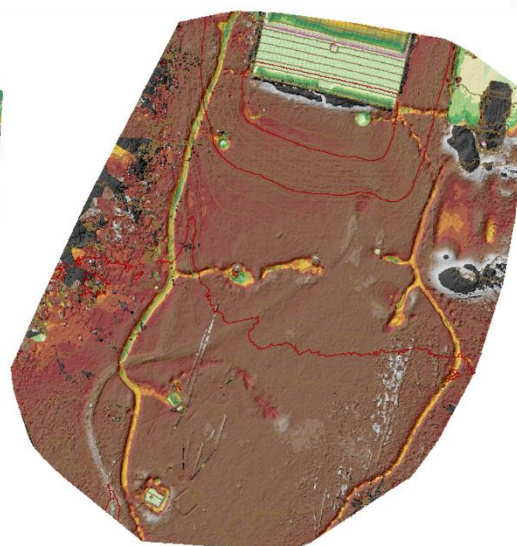
12/03   19/03
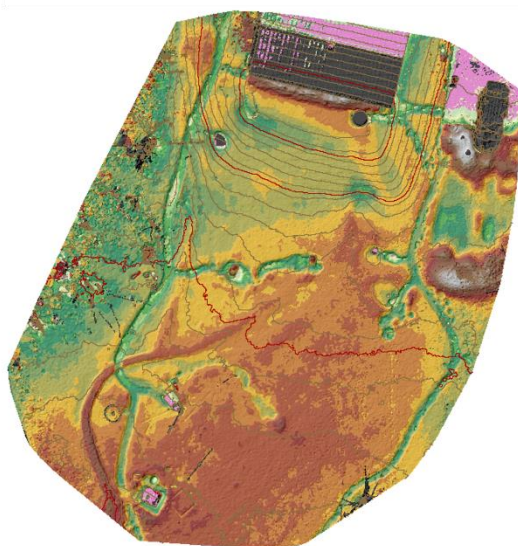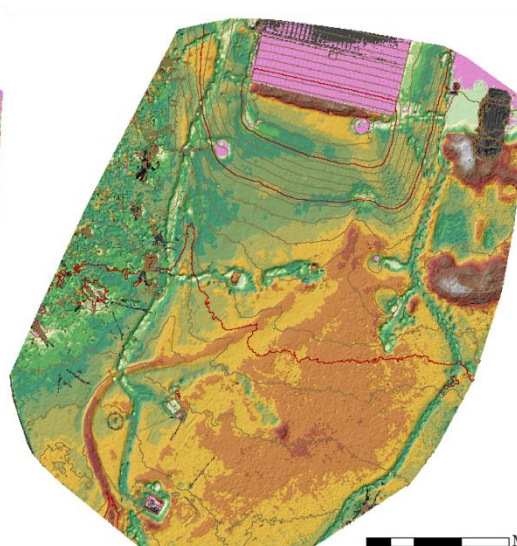
Figure 3: Snow depth calculated by photogrammetry for the four dates covered in this study.
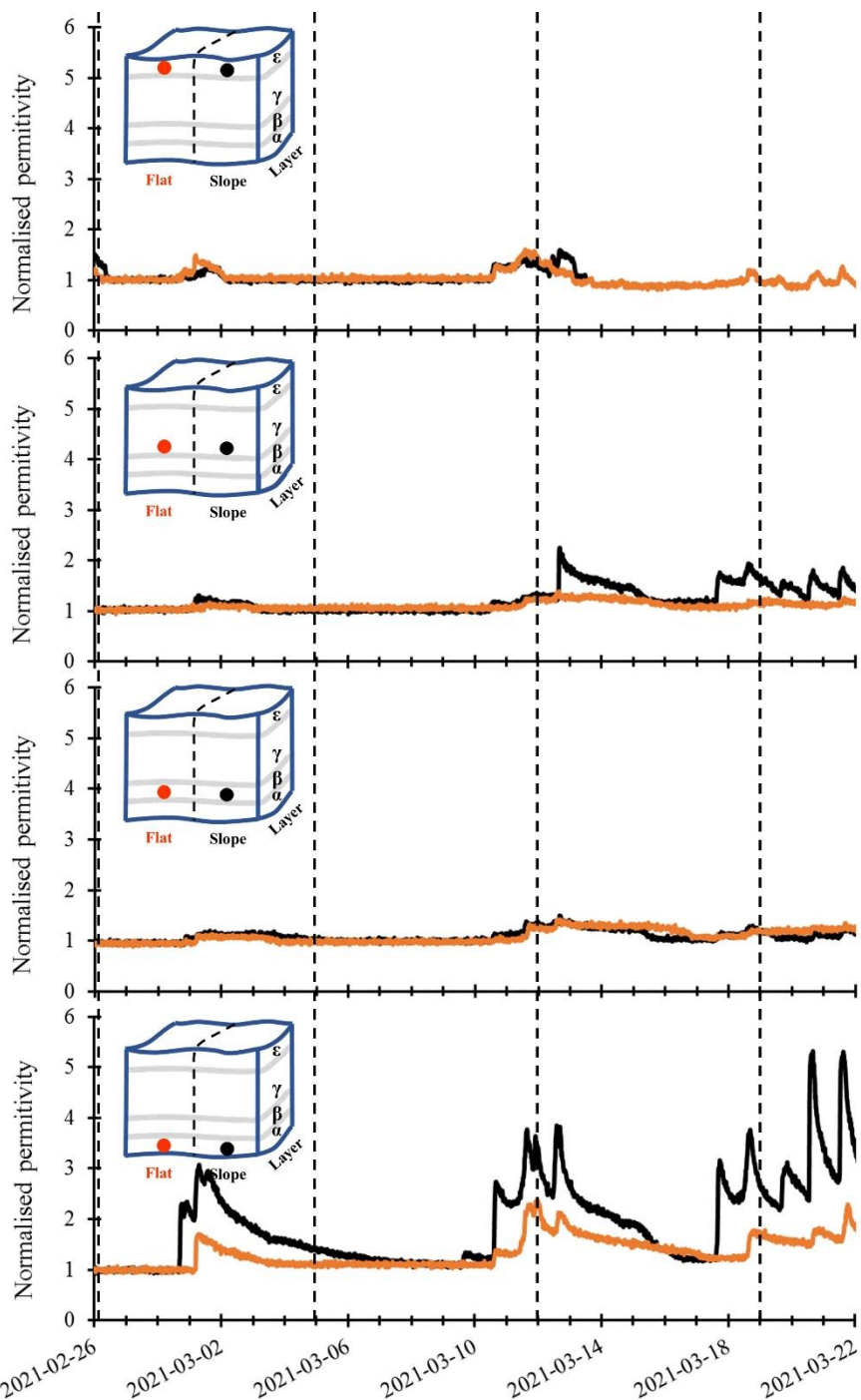
590

Figure 4: Normalized permittivity measured by TDR probes in the sloped and flat sections. Probe positions in each graph are shown in drawings representing a simplified description of the snowpack. Vertical dashed lines mark field visit dates.
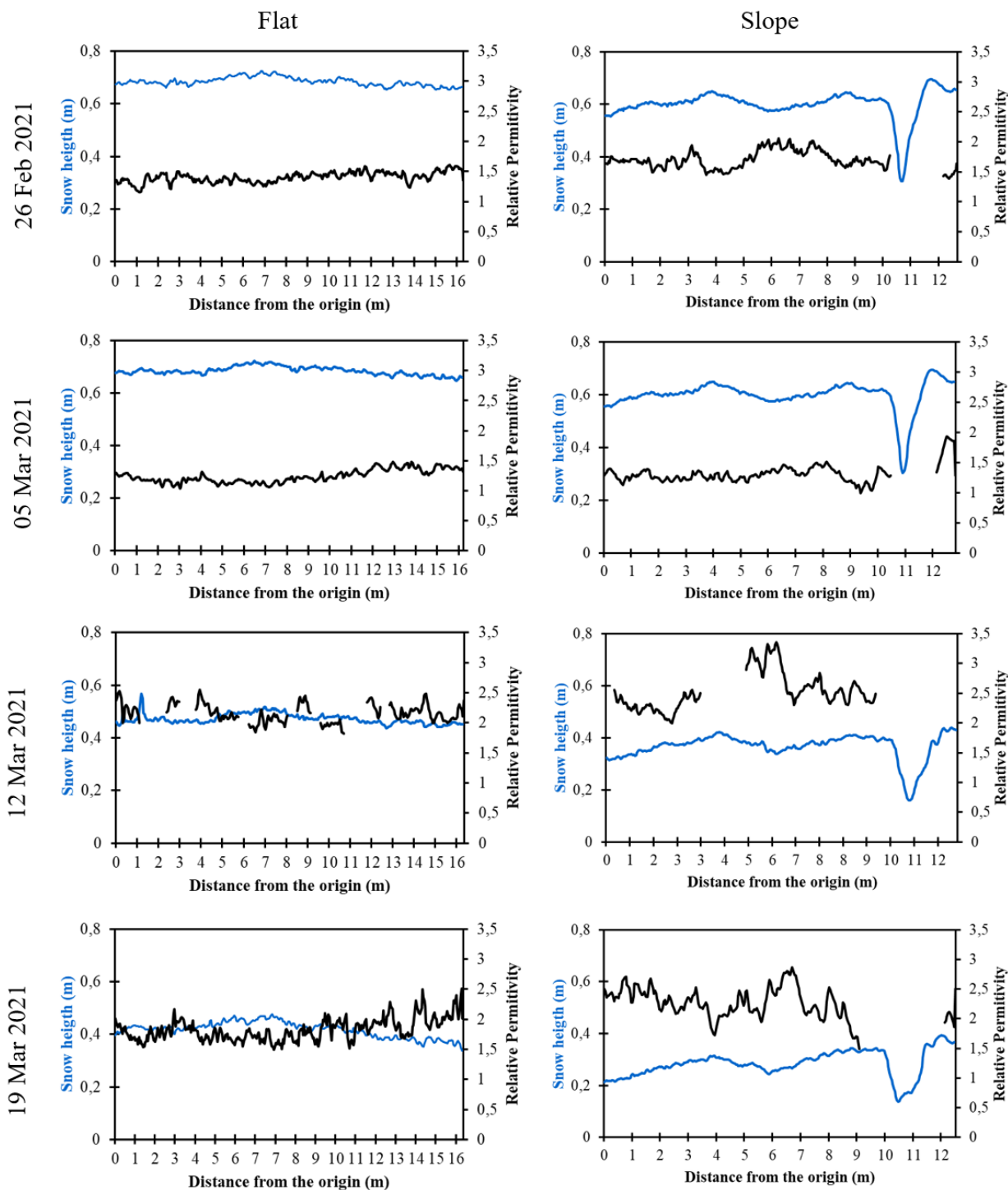
Figure 5: Bulk permittivity and snow depth calculated for the flat and slope transects on February 26, March 5, March 12 and
595 **March 19. Adapted from Valence and Baraer (2021).**
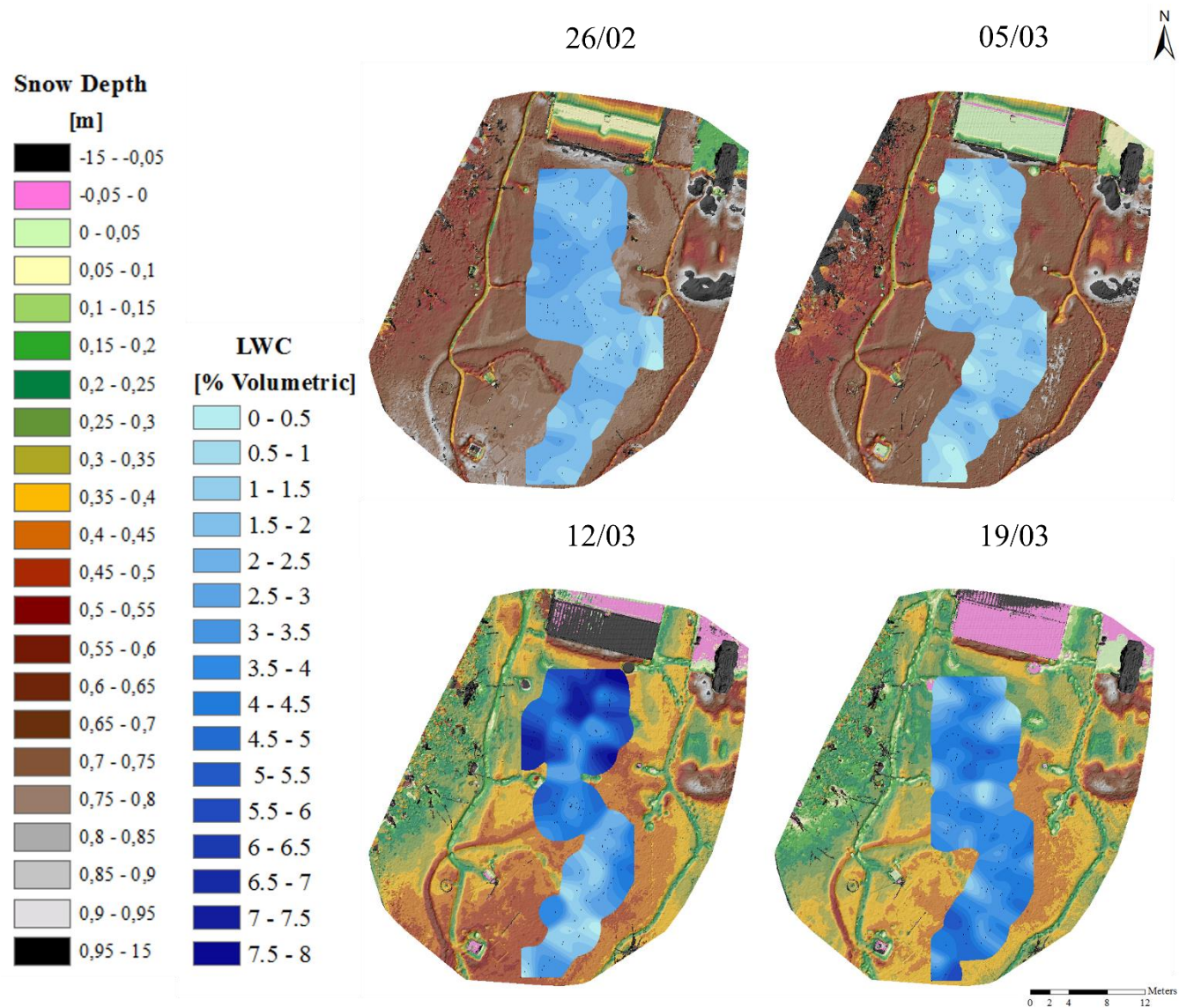
Figure 6: LWC calculated by GPR frequency dependent attenuation analysis.
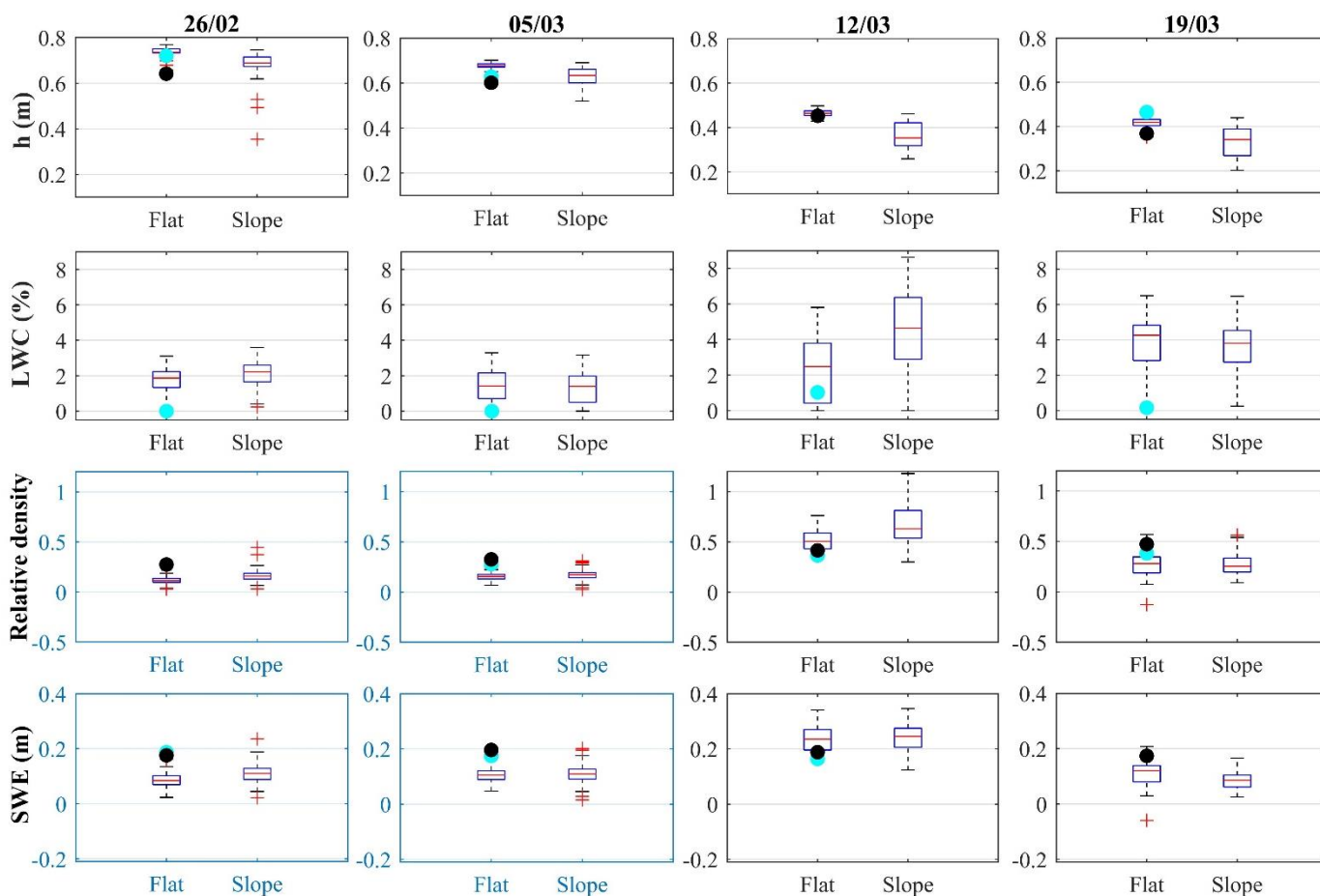
Figure 7: Box plots representing the snowpack studied variables for the sloped and flat areas for each survey date. In the boxes, the central red line represents the median, and the bottom and top blue edges mark the 25th and 75th percentiles, respectively. The whiskers show the data ranges excluding outliers. Wherever existing, outliers are represented by a red cross. Circle markers represent reference values originating from the AWS (in blue) and snow pits (in black). Figures framed in blue were created with the assumption of a dry snowpack.

Table 1: List of the instruments used in this study. Accuracy is either given by the manufacturer or estimated for worst-case scenarios.
Adapted from Paquotte and Baraer (2022).

Variable	Sensors	Manufacturer	Accuracy	Timestamp
T_{air}	Hygrovue10	Campbell Scientific	±0.6°C	15 min
Precipitation	From P.E.T. station		±4.5%	15 min
h	Ultrasonic (SR50A)	Campbell Scientific	±1 cm	15 min
$T_{n,cm}$	Thermal profiler (CS230)	Campbell Scientific	±0.2°C	15 min
Outflow	Lysimeter	Homemade	±1%	15 min
SWE	SWE sensor (CS725)	Campbell Scientific	±15 mm	6 h
Permittivity (ε)	TDR (CS610)	Campbell Scientific	±5%	15 min

610

Table 2: Methods combined in this study classified based on the sampling frequency and the spatial coverage.

Variable	Continuous, single point	Repetitive, single point	Repetitive, two surfaces
h	Sonic sensor	Snow pit	Photogrammetry
ρ	h / SWE	Snow pit	GPR
SWE	SWE sensor	Snow pit	GPR
LWC	TDR (2 points, 4 layers)	A2	GPR